Strongly enhanced Rashba splittings in an oxide heterostructure: A tantalate monolayer on BaHfO_{3}

Minsung Kim, Jisoon Ihm, and Suk Bum Chung

Phys. Rev. B **94**, 115431 — Published 22 September 2016

DOI: 10.1103/PhysRevB.94.115431

Strongly enhanced Rashba splittings in an oxide heterostructure: a tantalate monolayer on $BaHfO_3$

Minsung Kim,[1,2] Jisoon Ihm,[1,*] and Suk Bum Chung[1,3,*]

[1] *Department of Physics and Astronomy, Seoul National University, Seoul 151-747, Korea*
[2] *Ames Laboratory, US DOE and Department of Physics and Astronomy, Iowa State University, Ames, Iowa 50011, USA*
[3] *Center for Correlated Electron Systems, Institute for Basic Science (IBS), Seoul 151-747, Korea*

(Dated: August 15, 2016)

In the two-dimensional electron gas emerging at the transition metal oxide surface and interface, various exotic electronic ordering and topological phases can become experimentally more accessible with the stronger Rashba spin-orbit interaction. Here, we present a promising route to realize significant Rashba-type band splitting using a thin film heterostructure. Based on first-principles methods and analytic model analyses, a tantalate monolayer on $BaHfO_3$ is shown to host two-dimensional bands originating from Ta t_{2g} states with strong Rashba spin splittings, nearly 10% of the bandwidth, at both the band minima and saddle points. An important factor in this enhanced splitting is the significant t_{2g}-e_g interband coupling, which can generically arise when the inversion symmetry is maximally broken due to the strong confinement of the 2DEG on a transition metal oxide surface. Our results could be useful in realizing topological superconductivity at oxide surfaces.

I. INTRODUCTION

Recently, the spin-orbit interaction of the two-dimensional electron gas (2DEG) at the surfaces and interfaces of the perovskite transition metal (TM) oxide [1–5] has been much investigated experimentally[6–12]. However, definite understanding on how its magnitude might be maximized has not been well established. It is the combination of the broken inversion symmetry and the atomic spin-orbit coupling (SOC) of the TM that gives rise to a non-zero spin splitting in the form of the Rashba spin-orbit interaction[13–15]. But this origin implies that the magnitude of the spin-orbit interaction is intrinsically limited by the TM atomic SOC. The limitation should be apparent in the best-studied perovskite 2DEGs — the $SrTiO_3$ (STO) surface and the $LaAlO_3/SrTiO_3$ (LAO/STO) heterostructure interface — as the atomic SOC strength of the 3d TM Ti is relatively small[16–18]. Experimental evidences have been mixed, with the claims of large magnitude stemming from the magnetoresistance measurements [6–10] contradicted by the Hanle effect measurement[11] as well as the measurement of similar magnetoresistance in the inversion-symmetric δ-doped STO heterostructure[12]. Meanwhile, theoretical calculations show the splitting near the Γ point to be two orders of magnitude smaller than the bandwidth at the best [16,18,19]. One natural way to overcome this limitation is adopting 5d TM oxides, such as tantalate, with a stronger atomic SOC. This has motivated the recent experiments on the 2DEG at the surface of $KTaO_3$ (KTO)[9,10].

However, the experiments on KTO have suggested that another important condition for enhancing the surface 2DEG Rashba spin-orbit interaction is to have the density profile of the surface state concentrated to the surface-terminating layer, which maximizes the effect of the broken inversion symmetry. The ARPES measurements on the KTO surface have seen no measurable spin splitting[9,10], in spite of not only the stronger SOC of Ta but also the polar nature of KTO (001) surface. According to a density functional theory (DFT) calculation[20], the surface state penetrates deeply into the bulk as the surface confinement potential is made shallow by the atomic relaxation near the surface layer. This suppresses the effect of the inversion symmetry breaking (ISB) on the surface state (which can be quantified by various parameters, *e.g.* the chiral orbital angular momentum coefficient[18,21–23]), and hence significantly reduces the Rashba spin-orbit interaction.

In this study, we have theoretically constructed a realistic oxide heterostructure that has a surface 2DEG with a strong Rashba spin-orbit interaction. Our idea is to consider a 5d TM oxide monolayer on a substrate, where 2DEG predominantly lies in the outermost monolayer film, maximizing the effect of the broken inversion symmetry from the substrate. Specifically, we attempt to replace the outer layers of perovskite oxide (001) surface with another perovskite thin film layers, in which the electronic bands of the substrate need to lie sufficiently far above the conduction band minimum (CBM) to make all essential low-energy physics originate from the thin film states near CBM. After calculations of a number of candidate perovskite oxides for the heterostructure, we find that TaO_2/KO (having Ta^{+5}) or TaO_2/BaO (having Ta^{+4}) layer on $BaHfO_3$ (001) surface (Fig. 1a) is a promising candidate structure possessing Ta t_{2g}-originated two-dimensional (2D) bands with a strong Rashba spin-orbit interaction. $BaHfO_3$ (BHO) is suitable as a substrate because its lattice structure (cubic at room temperature) matches with that of KTO, the only stable perovskite material containing TaO_2[24,25], and the alignment of its conduction bands and the Ta t_{2g} bands enables minimal hybridization. It should be emphasized that the concentration of the surface state in the outermost layer is an important condition to maximize the ISB effect. This confinement of the 2DEG to an atomic monolayer in our system is in sharp contrast to that of the LAO/STO heterostructure, where the 2DEG is merely

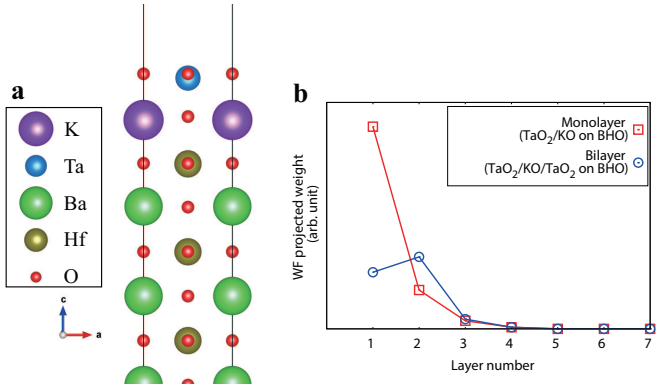

FIG. 1. Atomic structure of a tantalate layer on $BaHfO_3$ (001). (a) Atomic structure of TaO_2/KO on $BaHfO_3$ from first-principles calculations; note the height difference between Ta and O at the top layer. (b) Wave function weight projected on $d_{xz/yz}$ of TMs for the lowest $d_{xz/yz}$ Rashba band at Γ. The TM-O_2 layers are numbered starting from the outermost layer.

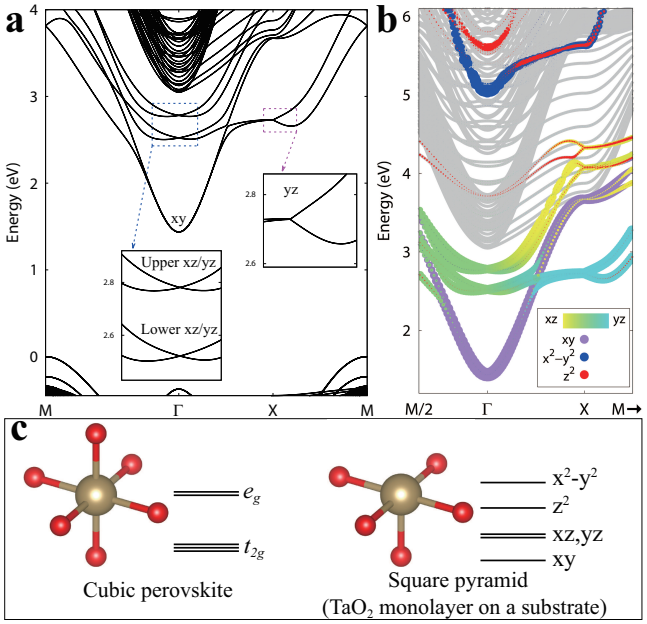

FIG. 2. Electronic structure of TaO_2/KO on $BaHfO_3$ from first-principles calculations. (a) Calculated band structure. (b) Projected weights of Ta d states. The Fermi level is set to the valence band maximum. (c) Schematic illustration of energy levels at Γ without SOC. The crystal field splitting of the monolayer-substrate heterostructure is different from that of the cubic (octahedral) case.

constrained to reside primarily on the STO (substrate) side. It is a key ingredient for the strongly enhanced Rashba splitting, as a weak confinement would give a negligible Rashba splitting even with the large atomic spin-orbit coupling. It is maximized with the monolayer; upon replaced by a bilayer (Fig. 1b), the surface state wave function no longer peaks at the outermost layer. We will also show that the t_{2g}-e_g coupling gives rise to the enhanced splitting not only at the band bottom but also at the band saddle points.

II. RESULTS

A. Rashba splitting near the Γ point

The electronic structures of TaO_2/KO monolayer (having Ta^{+5}) on BHO (lattice constant ≈ 4.155 Å) from our first-principles calculations using DFT as implemented in VASP[26,27] are presented in Fig. 2 (see Appendix A for details). The bands near the CBM consist of t_{2g} (d_{xy}, d_{xz}, d_{yz}) states of Ta in the outermost layer, with the calculated bandwidth of ≈ 1.7 eV for the $d_{xz/yz}$ bands. These bands being 2D, the triple degeneracy (excluding spin) of the t_{2g} bands at Γ is lifted, splitting the d_{xy} and the $d_{xz/yz}$ manifolds; the Ta atomic SOC further splits the $d_{xz/yz}$ bands into upper and lower $d_{xz/yz}$ states. Finally, when the ISB at the surface is accounted for, the Rasha-type band splitting lifts spin degeneracies in the entire Brillouin zone (BZ) except at the time-reversal invariant momenta Γ, X and M. We note that this Rashba-type band splitting of the $d_{xz/yz}$ bands is strikingly larger in magnitude than that of the d_{xy} bands, contrary to the prediction of the t_{2g}-only model[19,28,29]. Moreover, our calculation gives the Rashba coefficient of the lower $d_{xz/yz}$ bands at Γ of $\alpha_R \approx 0.3$ eVÅ, which is an order of magnitude larger than that of LAO/STO heterostructure deduced from the experimental magnetoresistance data[7], and the Rashba energy of $E_R \gtrsim 15$ meV; these values are also significantly larger than $\alpha_R \approx 0.1$ eVÅ, $E_R \approx 1$ meV for the bilayer case of Fig. 1b. The Rashba-Dresselhaus effect along the BZ boundary is even more pronounced, with a giant splitting (≈ 180 meV), which is nearly twice the maximum reported value[8] in the perovskite oxide 2DEG, occurring near X along $k_{x/y} = \pi$.

An analysis that includes all Ta d-orbitals – not only the t_{2g} orbitals but also the e_g orbitals – is required to understand the two conspicuous features of Fig. 2, the discrepancy between the Rashba splitting of the d_{xy} and the $d_{xz/yz}$ bands, and the giant splitting along $k_{x/y} = \pi$. We employ an analytic TB model for a qualitative analysis and supplement it with quantitative results from maximally localized Wannier functions (MLWFs). In the TB model, we consider a Hamiltonian for all Ta d-orbitals, including the e_g orbitals (d_{z^2}, $d_{x^2-y^2}$) in a square lattice[20,30] to describe the TaO_2 layer 2D bands,

$$\mathcal{H} = \mathcal{H}_{\rm hop} + \mathcal{H}_{\rm SOC} + \mathcal{H}_{\rm E} + \mathcal{V}_{\rm sf}, \qquad (1)$$

where the first term $\mathcal{H}_{\rm hop}$ describes the nearest-neighbor hopping, and the second term $\mathcal{H}_{\rm SOC} = \xi \mathbf{L}\cdot\mathbf{S}$ is the atomic SOC, with $\xi \approx 0.26$ eV for Ta. The third term $\mathcal{H}_{\rm E}$ includes the additional hoppings that would have been for-

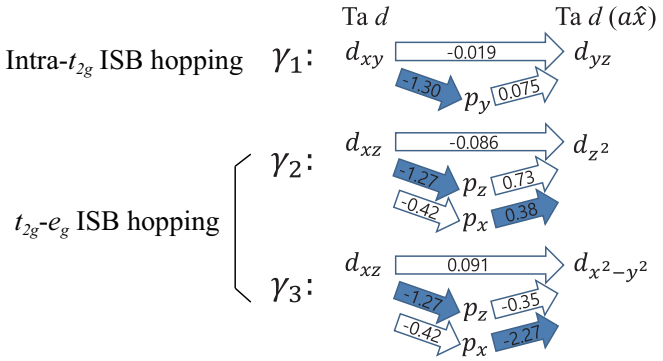

FIG. 3. Hopping strengths (in eV) between Wannier functions for Ta d states at one site and the neighboring site in the x-direction. Both direct (horizontal arrows) and indirect (oblique arrows, via O p) paths are depicted. Empty arrows indicate terms that would be absent without ISB.

bidden if not for the ISB:

$$\begin{aligned}\gamma_1 &= \langle d_{xy}|\mathcal{H}_{\rm E}|d_{xz}\rangle_{\hat{y}} = \langle d_{xy}|\mathcal{H}_{\rm E}|d_{yz}\rangle_{\hat{x}}\\ \gamma_2 &= \langle d_{xz}|\mathcal{H}_{\rm E}|d_{z^2}\rangle_{\hat{x}} = \langle d_{yz}|\mathcal{H}_{\rm E}|d_{z^2}\rangle_{\hat{y}}\\ \gamma_3 &= \langle d_{x^2-y^2}|\mathcal{H}_{\rm E}|d_{yz}\rangle_{\hat{y}} = \langle d_{xz}|\mathcal{H}_{\rm E}|d_{x^2-y^2}\rangle_{\hat{x}},\end{aligned} \tag{2}$$

in which the vectors in the subscripts denote the relative position of the two orbitals with the lattice constant set to 1 for convenience (these ISB hoppings play a role analogous to the chiral orbital angular momentum effect in the p-orbital bands[21–23]). Here, γ_1 is the intra-t_{2g} ISB hopping while γ_2 and γ_3 describe t_{2g}-e_g ISB hoppings. The fourth term $\mathcal{V}_{\rm sf}$ describes the potential difference due to the surface field. By deriving the effective Hamiltonian $\mathcal{H}_{eff}$ that acts on each two-fold degenerate band in the weak SOC limit where $\mathcal{H}_{\rm hop}+\mathcal{V}_{\rm sf}$ is dominant over $\mathcal{H}_{\rm SOC}$, we obtain Rashba-type band splitting terms near Γ and X as summarized in Table I (see Appendix B for details). Table I shows the Rashba coupling to be linear in the ISB hopping $\gamma_{1,2,3}$ divided by the energy difference between two relevant states Δ.

One reason why the e_g orbital contribution is crucial for the Rashba splitting in the t_{2g} bands is that the t_{2g}-e_g ISB hoppings $\gamma_{2,3}$ are significantly larger than the intra-t_{2g} hopping γ_1: $\gamma_1 \approx -0.04$ eV, $\gamma_2 \approx -0.25$ eV, $\gamma_3 \approx 0.30$ eV. This is a necessary condition for the effective Hamiltonian of Table I to give larger Rashba splittings in the $d_{xz/yz}$ bands than d_{xy} as shown in Fig. 2, given that the $d_{xz/yz}$ bands are closer in energy to the d_{xy} band than the e_g bands (albeit within an order of magnitude). The inclusion of the O p states in our MLWF analysis can clarify the microscopic physics behind this result. Examining the hopping parameters relevant to γ_1, the particularly small ISB hopping between O p_y and Ta d_{yz} along x direction (Fig. 3) can be attributed to the relative positions and shapes of the two orbitals; the lobes of the two orbitals lie on the yz plane that is perpendicular to the hopping direction ($\hat{x}$), and p_y has maximum amplitude along y direction whereas d_{yz} has a node along it. Thus, we have the negligible Rashba splitting of the d_{xy} band as shown in Fig. 2, despite the smaller energy difference with the $d_{xz/yz}$ bands.

TABLE I. Splitting terms of the effective Hamiltonian $\mathcal{H}_{eff}$ for Ta t_{2g} manifolds. $\vec{k}$ denotes the reference point of the effective Hamiltonian with $\Gamma = (0,0)$ and $\mathrm{X} = (\pi, 0)$. $\Delta(\tilde{\Delta})$ represents the energy difference between the states in the subscript at Γ(X), where uxz/yz and lxz/yz mean the upper xz/yz and the lower xz/yz, respectively.

$\vec{k}$	Manifold	Splitting terms in $\mathcal{H}_{\rm eff}$
Γ	upper $d_{xz/yz}$	$\left[\frac{-2\gamma_3\xi}{\Delta_{uxz/yz,x^2-y^2}} + \frac{-2\gamma_1\xi}{\Delta_{uxz/yz,xy}}\right](\vec{\sigma}\times\vec{k})\cdot\hat{z}$
	lower $d_{xz/yz}$	$\frac{2\sqrt{3}\gamma_2\xi}{\Delta_{lxz/yz,z^2}}(\vec{\sigma}\times\vec{k})\cdot\hat{z}$
	d_{xy}	$\frac{-2\gamma_1\xi}{\Delta_{xy,uxz/yz}}(\vec{\sigma}\times\vec{k})\cdot\hat{z}$
X	d_{yz}	$\left[\frac{-2\sqrt{3}\gamma_2\xi}{\tilde{\Delta}_{yz,z^2}} + \frac{2\gamma_3\xi}{\tilde{\Delta}_{yz,x^2-y^2}}\right]\sigma_x k_y - \frac{2\gamma_1\xi}{\tilde{\Delta}_{yz,xy}}\sigma_y k_x$

The other reason why the e_g orbital contribution is crucial for the Rashba splitting in the t_{2g} bands is the reduced t_{2g}-e_g energy splitting. Indeed, when the t_{2g}-e_g energy splitting is set to be infinite in Table I, all the results from the t_{2g}-only TB models[17–19,28,29] are recovered, including the absence of k-linear Rashba in the lower $d_{xz/yz}$ band near Γ. In the case of 3D cubic KTO, the t_{2g}-e_g energy separation at Γ is calculated to be ≈ 4.6 eV, which is larger than that of our system (Fig. 2a, b). Compared with the 3D cubic bulk case, Figure 2b shows considerable portion of d_{z^2} states close in energy, *i.e.*, less than bandwidth, to the t_{2g} bands; this is due to the absence of an O atom in one of the octahedral points surrounding Ta. Hence, as shown in Fig. 2c, the local atomic configuration for the Ta atom is close to a square pyramid, where the d_{z^2} and lower $d_{xz/yz}$ are close in energy. This can be taken as a generic result for the case where the 2DEG wave function is confined almost entirely to the outermost layer. The height difference of Ta and O atoms (≈ 0.20 Å) in the TaO_2 layer enhances the t_{2g}-e_g coupling in both ways; the larger effect being the enhancement of the ISB hopping γ_3, but there is also noticeable lowering of the $d_{x^2-y^2}$ orbital energy level.

The t_{2g}-e_g coupling also plays a key role in determining the angular momentum (AM) texture of the t_{2g} bands in close vicinity of Γ (Fig. 4). The tetragonal crystal field and the SOC determine the spin-orbital entanglement of the band manifolds: the spin-up and spin-down are in nearly the same orbital state for the d_{xy} bands while they are in nearly orthogonal orbital states for the $d_{xz/yz}$ bands. This entanglement affects the AM character; the spin AM is dominant in the d_{xy} bands whereas the orbital AM is dominant[18,21,22] in the $d_{xz/yz}$ bands (see Appendix B for details). The t_{2g}-e_g coupling gives a nonzero AM in the lower $d_{xz/yz}$ bands, contrary to the t_{2g}-only TB model, and quantitatively changes the AM in the upper $d_{xz/yz}$.

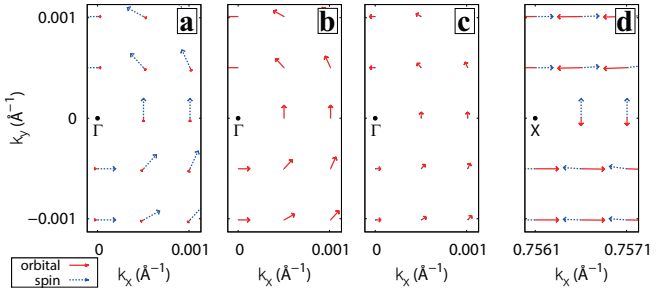

FIG. 4. Angular momentum texture from first-principles calculations in close vicinity of Γ and X. Orbital and spin angular momenta are presented for the lower Rashba band of (a) the d_{xy}, (b) the lower $d_{xz/yz}$, and (c) the upper $d_{xz/yz}$ bands near Γ, and the lower Rashba-Dresselhaus band of the (d) d_{yz} bands near X = $(\pi, 0)$

.

B. Band splitting near the X point

As shown in Table I, the lowered symmetry C_{2v} at X allows the mixture of Rashba and linear Dresselhaus terms in general (see Appendix B for details), with the linear Dresselhaus larger in magnitude as shown in Fig. 4d. Due to the anisotropic dispersion of $d_{xz/yz}$ bands, the lowest conduction band at X = $(\pi, 0)$ mainly consists of d_{yz} state. We find that the larger band splitting along X—M comes from the t_{2g}-e_g coupling whereas the smaller splitting along X—Γ is due to the intra-t_{2g} coupling. Hence, the giant Rashba-Dresselhaus splitting in vicinity of X (≈ 180 meV) is due to the e_g contribution. It has been recently pointed out[31] that this Rashba-Dresselhaus splitting along X—M is necessary for weak topological superconductivity, which gives rise to dislocation Majorana zero modes. The Rashba-Dresselhaus splitting near X also splits the logarithmic van Hove singularity (VHS) of the $d_{xz/yz}$ band saddle point, which means that the new VHSs do not have spin degeneracy and occur away from X (see Appendix C for details). While the enhancement of the superconducting instability from the logarithmic VHS at X is possible only for the spin-singlet channel[32–36], it was recently shown[37–39] that the logarithmic VHS away from X can enhance the instability to the spin-triplet p-wave superconductivity. The physics at X is experimentally accessible through the chemical substitution we will discuss below.

C. Electron doping

To actually realize the 2DEG in the TaO_2 layer, electron doping is needed because the nominal charge of the TaO_2 layer is +1 and that of the KO layer is -1 (BaO and HfO_2 layers are neutral.). One possible way would be substituting K atoms with Ba in the KO layer. In this case, the Rashba strength remains still large ($\alpha_R \approx 0.2$ eVÅ) in the lower $d_{xz/yz}$ bands (Fig. 5a), while the

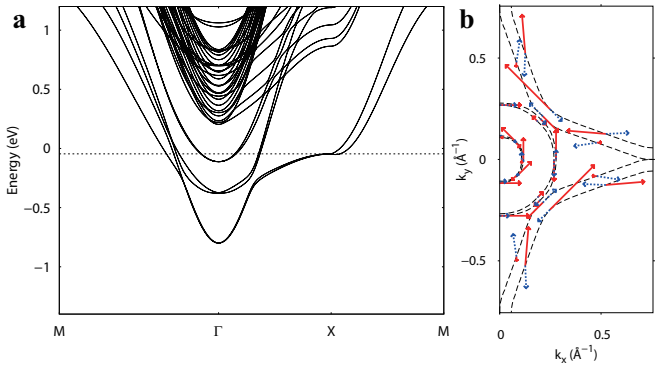

FIG. 5. Electronic structure of a TaO_2 layer on BaO-terminated $BaHfO_3$ (001) from first-principles calculations. (a) Band structure. The dotted horizontal line denotes the energy level of the VHS in absence of the Rashba-Dresselhaus splitting, E_{vH}, with the Fermi level set to 0. (b) AM texture at E_{vH} with constant energy lines. The red and blue arrows correspond to the orbital and spin AM, respectively.

Rashba splitting in the upper $d_{xz/yz}$ bands is greatly suppressed largely because the Ba substitution reduces by 70% the height difference of Ta and O atoms in the TaO_2 layer. This means that, for the Rashba effect in the lower $d_{xz/yz}$ band, the sharp 2DEG confinement is as much important as the lattice distortion. Also, it needs to be noted that the strong confinement is a prerequisite for the Rashba strength enhancement by the polar distortion since the polar distortion at the outermost layer will be effective in the Rashba enhancement only when the 2DEG is sufficiently confined to that layer. Once again, the considerable band splitting along X–M (≈ 24 meV) and AM texture at E_{vH} in Fig. 5 are contrary to the prediction of the t_{2g}-only TB model (see Appendix D for details), and hence demonstrate that inclusion of the e_g manifold is essential in understanding the Rashba-Dresselhaus splitting. We expect that partial chemical substitution ($TaO_2/K_{1-x}Ba_xO$ layer on BHO) could induce the 2DEG in the TaO_2 layer in experiments. The VHS is accessible at $x \lesssim 1$, *i.e.* 100% Ba substitution (Fig. 5a).

III. CONCLUSION

We expect the qualitative features of our Rashba-Dresselhaus splitting to be generic, rather than material specific, for the (001) perovskite transition metal oxide 2DEG with maximal ISB, where the 2DEG wave function profile is required to be concentrated on the surface-terminating TM-O_2 layer. In general, the substrate is required to have a good lattice match and the minimal overlap with the Ta t_{2g} bands; the former ruled out $BaZrO_3$ and the latter $SrTiO_3$ as an alternative substrate. It is also found that compressive strain on the BHO substrate, a possible necessity for the feasible deposition of

the thin film due to relatively large lattice mismatch between KTO and BHO, does not substantially affect the band splitting (see Appendix E for details). Considering that 2DEG in an artificial film-substrate system has been realized experimentally in $SrVO_3$ thin films on Nb-doped STO[40], we expect our system to be experimentally realized using the state-of-the-art layer-by-layer growth control of perovskite oxide thin films[41]. The recent report of the $SrHfO_3$ film grown by molecular beam epitaxy[42] suggests that fabricating heterostructures with refractory $5d$ metals may not be beyond current technology. The spin and orbital AM texture of our system may be experimentally detectable through its optical response[43,44].

IV. ACKNOWLEDGMENTS

We thank Jung Hoon Han, Changyoung Kim, Choong-Hyun Kim, Hyeong-Do Kim, Minu Kim, Hyun-Woo Lee, Hosub Jin, Seung Ryong Park, Cai-Zhuang Wang, Hong Yao and Jaejun Yu for fruitful discussions and comments. This work was supported by the NRF of Korea Grant No. 2006-0093853 (M.K., J.I.) and IBS-R009-Y1 (S.B.C.). Research at Ames laboratory (M.K.) was supported by the US DOE, Office of Basic Energy Sciences, Division of Materials Sciences and Engineering under Contract No. DE-AC02-07CH11358. Computations were performed through the support of KISTI, and NERSC in Berkeley, CA.

Appendix A: Details of the first-principles calculations

We performed density functional theory calculations as implemented in VASP[26,27]. Projector augmented-wave method was used[45]. A plane-wave basis set with the cutoff energy 520 eV was employed, and PBEsol (Perdew-Burke-Ernzerhof revised for solids) exchange-correlation functional was adoped[46]. We employed a symmetric slab configuration with 15 HfO_2 and 14 BaO layers between 2 TaO_2/KO layers for the electronic band structure of the monolayer-substrate heterostructure. The vacuum region of approximately 24Å was used to prevent the unwanted interaction between the periodic slab images. All lattice relaxations along the (001) direction are accounted for, as we used the lattice constant optimized in bulk calculations of $BaHfO_3$ and the internal atomic positions were fully relaxed until the force became less than 0.01 eV/Å. The band alignment obtained from these calculations, with the Ta t_{2g} bands lying well below Hf $5d$ bands, is qualitatively reliable as the experimental band gap of $BaHfO_3$ ($\sim$5.4 eV) is much larger than that of $KTaO_3$ ($\sim$3.6 eV) and the oxygen p-band of the TaO_2 layer lies only $\sim$0.24 eV below the valence band maximum. We employed maximally localized Wannier functions[47–49] to further analyze the results of the first-principles calculations. The Wannier functions were constructed for d orbitals of Ta in one set, and p orbitals of three neighboring O as well as d orbitals of Ta in the other set.

The 2DEG density can be affected by contamination of the clean surface. In $KTaO_3$, the TaO_2-terminated surface could contain approximately half a KO layer on it to compensate for $0.5e^-$ per unit cell, and the partial KO coverage could be controlled by UV irradiation[10]. On the other hand, in our structural model of TaO_2/KO on $BaHfO_3$, the nominal charge of the $(TaO_2)^+$ layer is compensated by the $(KO)^-$ layer. In TaO_2/BaO on $BaHfO_3$, some contamination could exist transforming Ta^{4+} to Ta^{5+}, which should be controlled to have the desired 2DEG density. Some alloy involving Ba and Hf could also affect the doping while it would not alter the electronic band structure significantly.

Appendix B: Tight-binding model for the TaO_2 film

We consider the tight-binding Hamiltonian for a TaO_2 film (d-orbitals in a square lattice)[30],

$$\mathcal{H} = \mathcal{H}_{\rm hop} + \mathcal{H}_{\rm SOC} + \mathcal{H}_{\rm E} + \mathcal{V}_{\rm sf},$$

where $\mathcal{H}_{\rm hop}$ describes the hopping between the nearest neighbors, $\mathcal{H}_{\rm SOC}$ is the atomic spin-orbit coupling of Ta, $\mathcal{H}_{\rm E}$ describes the orbital mixing due to the inversion symmetry breaking field near the surface, and $\mathcal{V}_{\rm sf}$ describes onsite

potential changes due to the surface field. Specifically, the hopping term is given by

$$\mathcal{H}_{\rm hop}=\begin{pmatrix} \frac{t_\sigma+3t_\delta}{2}(c_x+c_y) & -\frac{\sqrt{3}}{2}(t_\sigma-t_\delta)(c_x-c_y) & 0 & 0 & 0 \\ -\frac{\sqrt{3}}{2}(t_\sigma-t_\delta)(c_x-c_y) & \frac{3t_\sigma+t_\delta}{2}(c_x+c_y) & 0 & 0 & 0 \\ 0 & 0 & 2t_\pi(c_x+c_y) & 0 & 0 \\ 0 & 0 & 0 & 2(t_\pi c_x+t_\delta c_y) & 0 \\ 0 & 0 & 0 & 0 & 2(t_\delta c_x+t_\pi c_y) \end{pmatrix},$$

where the basis is $\{|d_{z^2}\rangle, |d_{x^2-y^2}\rangle, |d_{xy}\rangle, |d_{xz}\rangle, |d_{yz}\rangle\}$, and t_σ, t_π, t_δ are hopping parameters between d-orbitals. c_x means $\cos k_x$. The lattice constant is set to 1. The spin-orbit coupling term is

$$\mathcal{H}_{\rm SOC}=\begin{pmatrix} 0 & 0 & 0 & 0 & 0 & 0 & 0 & -\frac{\sqrt{3}}{2}\xi & 0 & \frac{\sqrt{3}}{2}\xi i \\ 0 & 0 & 0 & 0 & 0 & 0 & \frac{\sqrt{3}}{2}\xi & 0 & \frac{\sqrt{3}}{2}\xi i & 0 \\ 0 & 0 & 0 & 0 & -\xi i & 0 & 0 & \frac{1}{2}\xi & 0 & \frac{1}{2}\xi i \\ 0 & 0 & 0 & 0 & 0 & \xi i & -\frac{1}{2}\xi & 0 & \frac{1}{2}\xi i & 0 \\ 0 & 0 & \xi i & 0 & 0 & 0 & 0 & -\frac{1}{2}\xi i & 0 & \frac{1}{2}\xi \\ 0 & 0 & 0 & -\xi i & 0 & 0 & -\frac{1}{2}\xi i & 0 & -\frac{1}{2}\xi & 0 \\ 0 & \frac{\sqrt{3}}{2}\xi & 0 & -\frac{1}{2}\xi & 0 & \frac{1}{2}\xi i & 0 & 0 & -\frac{1}{2}\xi i & 0 \\ -\frac{\sqrt{3}}{2}\xi & 0 & \frac{1}{2}\xi & 0 & \frac{1}{2}\xi i & 0 & 0 & 0 & 0 & \frac{1}{2}\xi i \\ 0 & -\frac{\sqrt{3}}{2}\xi i & 0 & -\frac{1}{2}\xi i & 0 & -\frac{1}{2}\xi & \frac{1}{2}\xi i & 0 & 0 & 0 \\ -\frac{\sqrt{3}}{2}\xi i & 0 & -\frac{1}{2}\xi i & 0 & \frac{1}{2}\xi & 0 & 0 & -\frac{1}{2}\xi i & 0 & 0 \end{pmatrix}.$$

The inversion symmetry breaking field terms are given by

$$\mathcal{H}_{\rm E}+\mathcal{V}_{\rm sf}=\begin{pmatrix} \delta_2 & 0 & 0 & -2i\gamma_2\sin k_x & -2i\gamma_2\sin k_y \\ 0 & \delta_3 & 0 & -2i\gamma_3\sin k_x & 2i\gamma_3\sin k_y \\ 0 & 0 & \delta_1 & 2i\gamma_1\sin k_y & 2i\gamma_1\sin k_x \\ 2i\gamma_2\sin k_x & 2i\gamma_3\sin k_x & -2i\gamma_1\sin k_y & 0 & 0 \\ 2i\gamma_2\sin k_y & -2i\gamma_3\sin k_y & -2i\gamma_1\sin k_x & 0 & 0 \end{pmatrix},$$

where

$$\begin{aligned} \delta_1 &= \varepsilon(d_{xy})-\varepsilon(d_{xz/yz}) \\ \delta_2 &= \varepsilon(d_{z^2})-\varepsilon(d_{xz/yz}) \\ \delta_3 &= \varepsilon(d_{x^2-y^2})-\varepsilon(d_{xz/yz}) \\ \gamma_1 &= \langle d_{xy}|\mathcal{H}_{\rm E}|d_{xz}\rangle_{\hat{y}}=\langle d_{xy}|\mathcal{H}_{\rm E}|d_{yz}\rangle_{\hat{x}} \\ \gamma_2 &= \langle d_{xz}|\mathcal{H}_{\rm E}|d_{z^2}\rangle_{\hat{x}}=\langle d_{yz}|\mathcal{H}_{\rm E}|d_{z^2}\rangle_{\hat{y}} \\ \gamma_3 &= \langle d_{x^2-y^2}|\mathcal{H}_{\rm E}|d_{yz}\rangle_{\hat{y}}=\langle d_{xz}|\mathcal{H}_{\rm E}|d_{x^2-y^2}\rangle_{\hat{x}}. \end{aligned}$$

The Hamiltonian near the Γ point can be written as

$$\mathcal{H}(\vec{k})\approx$$

$$\begin{pmatrix} \frac{t_\sigma+3t_\delta}{2}C+\delta_2 & 0 & -\frac{\sqrt{3}}{2}(t_\sigma-t_\delta)D & 0 & 0 & 0 & 0 & -\sqrt{2}\gamma_2(ik_x-k_y) & -\sqrt{\frac{3}{2}}\xi & -\sqrt{2}\gamma_2(ik_x+k_y) \\ 0 & \frac{t_\sigma+3t_\delta}{2}C+\delta_2 & 0 & -\frac{\sqrt{3}}{2}(t_\sigma-t_\delta)D & 0 & 0 & -\sqrt{2}\gamma_2(ik_x+k_y) & 0 & -\sqrt{2}\gamma_2(ik_x-k_y) & \sqrt{\frac{3}{2}}\xi \\ -\frac{\sqrt{3}}{2}(t_\sigma-t_\delta)D & 0 & \frac{3t_\sigma+t_\delta}{2}C+\delta_3 & 0 & -\xi i & 0 & \frac{1}{\sqrt{2}}\xi & -\sqrt{2}\gamma_3(ik_x+k_y) & 0 & -\sqrt{2}\gamma_3(ik_x-k_y) \\ 0 & -\frac{\sqrt{3}}{2}(t_\sigma-t_\delta)D & 0 & \frac{3t_\sigma+t_\delta}{2}C+\delta_3 & 0 & \xi i & -\sqrt{2}\gamma_3(ik_x-k_y) & -\frac{1}{\sqrt{2}}\xi & -\sqrt{2}\gamma_3(ik_x+k_y) & 0 \\ 0 & 0 & \xi i & 0 & 2t_\pi C+\delta_1 & 0 & -\frac{1}{\sqrt{2}}i\xi & \sqrt{2}i\gamma_1(ik_x+k_y) & 0 & -\sqrt{2}i\gamma_1(ik_x-k_y) \\ 0 & 0 & 0 & -\xi i & 0 & 2t_\pi C+\delta_1 & -\sqrt{2}i\gamma_1(ik_x-k_y) & -\frac{1}{\sqrt{2}}i\xi & \sqrt{2}i\gamma_1(ik_x+k_y) & 0 \\ 0 & \sqrt{2}\gamma_2(ik_x-k_y) & \frac{1}{\sqrt{2}}\xi & \sqrt{2}\gamma_3(ik_x+k_y) & \frac{1}{\sqrt{2}}i\xi & -\sqrt{2}i\gamma_1(ik_x+k_y) & (t_\pi+t_\delta)C+\frac{\xi}{2} & 0 & (t_\pi-t_\delta)D & 0 \\ \sqrt{2}\gamma_2(ik_x+k_y) & 0 & \sqrt{2}\gamma_3(ik_x-k_y) & -\frac{1}{\sqrt{2}}\xi & \sqrt{2}i\gamma_1(ik_x-k_y) & \frac{1}{\sqrt{2}}i\xi & 0 & (t_\pi+t_\delta)C+\frac{\xi}{2} & 0 & (t_\pi-t_\delta)D \\ -\sqrt{\frac{3}{2}}\xi & \sqrt{2}\gamma_2(ik_x+k_y) & 0 & \sqrt{2}\gamma_3(ik_x-k_y) & 0 & \sqrt{2}i\gamma_1(ik_x-k_y) & (t_\pi-t_\delta)D & 0 & (t_\pi+t_\delta)C-\frac{\xi}{2} & 0 \\ \sqrt{2}\gamma_2(ik_x-k_y) & \sqrt{\frac{3}{2}}\xi & \sqrt{2}\gamma_3(ik_x+k_y) & 0 & -\sqrt{2}i\gamma_1(ik_x+k_y) & 0 & 0 & (t_\pi-t_\delta)D & 0 & (t_\pi+t_\delta)C-\frac{\xi}{2} \end{pmatrix},$$

with $C=\cos k_x+\cos k_y\approx 2-\frac{k_x^2}{2}-\frac{k_y^2}{2}$, $D=\cos k_x-\cos k_y\approx -\frac{k_x^2}{2}+\frac{k_y^2}{2}$, where we performed a unitary transformation to diagonalize the $d_{xz/yz}$ subspace in the limit that the $d_{xz/yz}$ states are sufficiently far from other manifolds and $\vec{k}\to 0$.

The effective Hamiltonian can be obtained by projection onto the concerned manifold

$$\mathcal{H}_{\rm eff}=\mathcal{P}\mathcal{H}\mathcal{P}+\mathcal{P}\mathcal{H}\mathcal{Q}\frac{1}{\epsilon-\mathcal{Q}\mathcal{H}\mathcal{Q}}\mathcal{Q}\mathcal{H}\mathcal{P},$$

where $\mathcal{P}$ is the projection operator onto the relevant manifold and $\mathcal{Q} = 1 - \mathcal{P}$. For the d_{xy} bands, the effective Hamiltonian is

$$\mathcal{H}_{\text{eff}} \approx h_{xy}(\vec{k}) I_{2\times 2} + \frac{-2\gamma_1 \xi}{\Delta_{xy,uxz/yz}} (\vec{\sigma} \times \vec{k}) \cdot \hat{z},$$

where $\Delta_{xy,uxz/yz} = 4t_\pi + \delta_1 - \{2(t_\pi + t_\sigma) + \frac{\xi}{2}\}$, and the Pauli matrices describe the subspace defined by $\{|d_{xy}\uparrow\rangle, |d_{xy}\downarrow\rangle\}$. For the lower $d_{xz/yz}$ bands,

$$\mathcal{H}_{\text{eff}} \approx h_{lxz/yz}(\vec{k}) I_{2\times 2} + \frac{2\sqrt{3}\gamma_2 \xi}{\Delta_{lxz/yz,z^2}} (\vec{\sigma} \times \vec{k}) \cdot \hat{z},$$

where $\Delta_{lxz/yz,z^2} = 2(t_\pi + t_\delta) - \frac{\xi}{2} - \{t_\sigma + 3t_\delta + \delta_2\}$, and the Pauli matrices describe the subspace defined by $\{\frac{1}{\sqrt{2}}(|d_{xz}\downarrow\rangle + i|d_{yz}\downarrow\rangle), \frac{1}{\sqrt{2}}(|d_{xz}\uparrow\rangle - i|d_{yz}\uparrow\rangle)\}$. For the upper $d_{xz/yz}$ bands,

$$\mathcal{H}_{\text{eff}} \approx h_{uxz/yz}(\vec{k}) I_{2\times 2} + \left[\frac{-2\gamma_3 \xi}{\Delta_{uxz/yz,x^2-y^2}} + \frac{-2\gamma_1 \xi}{\Delta_{uxz/yz,xy}}\right] (\vec{\sigma} \times \vec{k}) \cdot \hat{z},$$

where $\Delta_{uxz/yz,x^2-y^2} = 2(t_\pi + t_\delta) + \frac{\xi}{2} - \{3t_\sigma + t_\delta + \delta_3\}$, $\Delta_{uxz/yz,xy} = 2(t_\pi + t_\delta) + \frac{\xi}{2} - \{4t_\pi + \delta_1\}$, and the Pauli matrices describe the subspace defined by $\{\frac{1}{\sqrt{2}}(|d_{xz}\downarrow\rangle - i|d_{yz}\downarrow\rangle), \frac{1}{\sqrt{2}}(|d_{xz}\uparrow\rangle + i|d_{yz}\uparrow\rangle)\}$.

The angular momentum (AM) texture can be calculated using the eigenstates with the lowest perturbative correction in ξ. For the d_{xy} manifold in close vicinity of the Γ point, the dominant spin AM expectation value $\langle S_y\rangle \approx \hbar/2$ for an eigenstate in x direction comes from the original d_{xy} manifold. The remnant orbital AM $\langle L_y\rangle \approx \hbar\xi/\Delta_{xy,uxz/yz}$ is due to the inter-band coupling to the upper $d_{xz/yz}$, which can be calculated using the eigenstate with the first-order correction in ξ that hybridizes the d_{xy} manifold with the upper $d_{xz/yz}$ and the $d_{x^2-y^2}$ manifolds. As for the lower $d_{xz/yz}$ manifold, both the orbital and spin AM expectation values

$$\langle L_y\rangle \approx \frac{-3\hbar\xi}{\Delta_{lxz/yz,z^2}} \tag{B1}$$

$$\langle S_y\rangle \approx -\frac{3}{4}\hbar \left(\frac{\xi}{\Delta_{lxz/yz,z^2}}\right)^2. \tag{B2}$$

for an eigenstate in x direction can be obtained only from the eigenstates with the first-order correction in ξ which leads to hybridization with the d_{z^2} manifold. Thus, the orbital dominant AM texture in the lower $d_{xz/yz}$ bands comes from the inter-band coupling to the d_{z^2}. Similarly, we find that the orbital dominant AM texture in the upper $d_{xz/yz}$ bands originates from the inter-band coupling to the d_{xy} and the $d_{x^2-y^2}$ manifolds.

Near the X $= (\pi, 0)$ point, the effective Hamiltonian is

$$\mathcal{H}_{\text{eff}} = h_{yz}(\vec{k}) I_{2\times 2} + \left[\frac{-2\sqrt{3}\gamma_2 \xi}{\tilde{\Delta}_{yz,z^2}} + \frac{2\gamma_3 \xi}{\tilde{\Delta}_{yz,x^2-y^2}}\right] \sigma_x k_y - \frac{2\gamma_1 \xi}{\tilde{\Delta}_{yz,xy}} \sigma_y k_x,$$

where $\tilde{\Delta}_{yz,z^2} = 2(t_\pi - t_\delta) - \delta_2$, $\tilde{\Delta}_{yz,x^2-y^2} = 2(t_\pi - t_\delta) - \delta_3$, $\tilde{\Delta}_{yz,xy} = 2(t_\pi - t_\delta) - \delta_1$, and the Pauli matrices describe the subspace defined by $\{|d_{yz}\uparrow\rangle, |d_{yz}\downarrow\rangle\}$, and (k_x, k_y) is a local coordinate with respect to $(\pi, 0)$. Here, the splitting terms are mixture of Rashba and linear Dresselhaus terms, which are of the form

$$\mathcal{H}_{\text{splitting}} = A\sigma_x k_y - B\sigma_y k_x,$$

with $A = \frac{-2\sqrt{3}\gamma_2\xi}{\tilde{\Delta}_{yz,z^2}} + \frac{2\gamma_3\xi}{\tilde{\Delta}_{yz,x^2-y^2}}$ and $B = \frac{2\gamma_1\xi}{\tilde{\Delta}_{yz,xy}}$. If we rotate the local coordinate by $\pi/4$ about k_z axis, the splitting terms become

$$\begin{aligned}\mathcal{H}_{\text{splitting}} &= \frac{A+B}{2}(\sigma_x k_y - \sigma_y k_x) + \frac{A-B}{2}(\sigma_x k_x - \sigma_y k_y) \\ &= \alpha_R(\sigma_x k_y - \sigma_y k_x) + \alpha_D(\sigma_x k_x - \sigma_y k_y).\end{aligned}$$

In our case, we have $|A| \gg |B|$, thus both Rashba and linear Dresselhaus terms are present with similar strength. Due to the symmetry, only Rashba term is allowed for C_{4v} at Γ (where we should have $A = B$), and both Rashba and linear Dresselhaus terms are allowed for C_{2v} at X[50].

Appendix C: The splitting of the log van Hove singularity at X

We show here that the Rashba-Dresselhaus splitting removes the spin degeneracy of the logarithmic van Hove singularity at X, resulting in the two separate logarithmic van Hove singularities for the upper and lower Rashba-Dresselhaus bands. This implies that there will be a divergent difference in the density of states change between the upper and lower Rashba-Dresselhaus bands, which would have a significant effect on the phase competition, *e.g.* through the relative magnitude of the pairing susceptibilities with different symmetries.

It is well-known that there is a logarithmic van Hove singularity at X in absence of the Rashba-Dresselhaus splitting. The dispersion of the lowest energy band near $\mathrm{X} = (\pi, 0)$ approximately follows the dispersion of the d_{yz} band,

$$\xi = 2(t_\delta \cos k_x + t_\pi \cos k_y) \approx t_\delta (k_x - \pi)^2 - t_\pi k_y^2 + 2(t_\pi - t_\delta);$$

it is well-understood that there is a logarithmic van Hove singularity at the saddle point of a quadratic Hamiltonian in 2D[51].

The addition of the Rashba-Dresselhaus term near X, $\mathcal{H}_{R-D} = A\sigma_x k_y - B\sigma_y(k_x - \pi)$, leads to the spin splitting of this saddle point, which modifies the dispersion to

$$\xi_\pm \approx t_\delta (k_x - \pi)^2 - t_\pi k_y^2 \pm \sqrt{A^2 k_y^2 + B^2 (k_x - \pi)^2} + 2(t_\pi - t_\delta).$$

Using the fact that the Fermi velocity vanishes when the van Hove singularity occurs, we can see that the van Hove singularity at $\mathrm{X} = (\pi, 0)$ is shifted to $(\pi \pm B/2t_\delta, 0)$ for the upper Rashba-Dresselhaus band, with the dispersion in its vicinity

$$\xi_+ \approx t_\delta \left(k_x - \pi \mp \frac{B}{2t_\delta}\right)^2 - \left(t_\pi + t_\delta \frac{A^2}{B^2}\right) k_y^2 + 2(t_\pi - t_\delta) - \frac{B^2}{4t_\delta}$$

and $(\pi, \pm A/2t_\pi)$ for the lower Rashba-Dresselhaus band, with the dispersion in its vicinity

$$\xi_- \approx \left(t_\delta + t_\pi \frac{B^2}{A^2}\right)(k_x - \pi)^2 - t_\pi (k_y \mp \frac{A}{2t_\pi})^2 + 2(t_\pi - t_\delta) + \frac{A^2}{4t_\pi}.$$

We see here that when we raise the chemical potential so that the Fermi surface passes through the X point, the Fermi level first passes through the logarithmic van Hove singularity of the lower Rashba-Dresselhaus band, and then that of the upper Rashba-Dresselhaus band.

Appendix D: The importance of e_g manifold in the angular momentum texture

Because the e_g manifold affects the Rashba-Dresselhaus splitting, the inclusion of the e_g manifold is important to correctly describe the AM texture. By numerically solving the tight-binding model, we obtained the AM expectation values with and without e_g manifold (Figure 6). For the t_{2g}-only limit, we set $\delta_2 \approx \delta_3 \approx 10^3$eV. We find considerable differences in view of the direction and magnitude of the AM. Notably, the coupling to e_g manifold has significant effects in the direction of the AM near X and in the intermediate region.

Appendix E: The effects of the strain

Due to the large lattice constant of $BaHfO_3$, it might be helpful to apply compressive strain to the substrate for the deposition of the tantalate thin film. The electronic band structure of TaO_2/KO layer on HfO_2-terminated $BaHfO_3$ with the lattice constant reduced by 2% is presented in Figure 7. We find that the Rashba coefficient remains still large (for example, $\alpha_R \approx 0.3$ eVÅ in the lower $d_{xz/yz}$ bands at Γ).

Although in this study, we assumed the tetragonal symmetry for our heterostructure, the $TaO_2/K_{1-x}Ba_xO$ layer on $BaHfO_3$, the tensile strain in the film due to the lattice mismatch induces an in-plane polar displacement in the TaO_2 layer in the $x \ll 1$ limit, which will give rise to anisotropy in the Rashba splitting. The VHS near the X is unaffected as this polarization vanishes in the $x = 1$ limit.

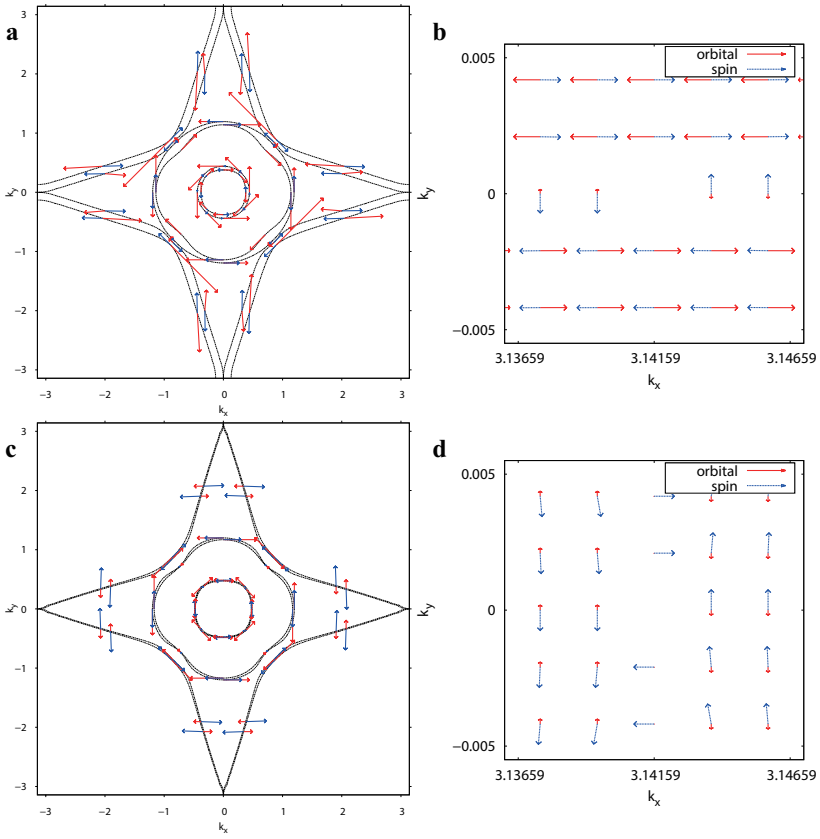

FIG. 6. Angular momentum texture from the tight-binding model. The angular momentum textures are calculated (a) at E_{vH} and (b) near X using both t_{2g} and e_g, and (c) at E_{vH} and (d) near X using only t_{2g}. The red and blue arrows represent the orbital and spin AM, respectively.

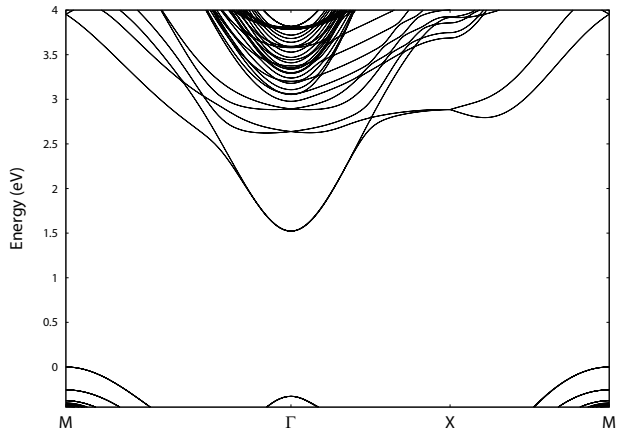

FIG. 7. Band structure of TaO_2/KO on HfO_2-terminated $BaHfO_3$ with the lattice constant reduced by 2%.

Appendix F: The relation between the band effective mass and Rashba-related parameters

Here, we show that both the momentum offset k_R and the Rashba energy E_R are proportional to the effective mass of the Rashba bands for a given Rashba strength α_R. We consider the Hamiltonian

$$\mathcal{H} = \frac{\hbar^2 k^2}{2m^*} I_{2\times 2} + \alpha_R(\vec{\sigma} \times \vec{k}) \cdot \hat{z},$$

with $k = \sqrt{k_x^2 + k_y^2}$, where m^* is the effective mass of the band and $I_{2\times2}$ is the 2×2 identity matrix. The energy dispersion of the lower Rashba band is given by

$$\begin{aligned} E(k) &= \frac{\hbar^2 k^2}{2m^*} - |\alpha_R| k \\ &= \frac{\hbar^2}{2m^*}(k - \frac{m^*|\alpha_R|}{\hbar^2})^2 - \frac{m^*|\alpha_R|^2}{2\hbar^2} \\ &\equiv \frac{\hbar^2}{2m^*}(k - k_R)^2 - E_R. \end{aligned}$$

We find that the momentum offset $k_R = \frac{m^*|\alpha_R|}{\hbar^2}$ and the Rashba energy $E_R = \frac{m^*|\alpha_R|^2}{2\hbar^2}$, which are principal measures of the band splitting size when one sees a band structure figure, are proportional to the effective mass m^* for a given Rashba parameter α_R. Thus, the Rashba splitting of the $d_{xz/yz}$ bands would look more pronounced due to the heavier effective mass compared with the d_{xy} band even if they had the same Rashba strength.

* To whom correspondence may be addressed. E-mail: jihm@snu.ac.kr, sbchung@snu.ac.kr

1. A. Ohtomo and H. Y. Hwang, Nature **427**, 423 (2004).
2. H. Takagi and H. Y. Hwang, Science **327**, 1601 (2010).
3. J. Mannhart and D. G. Schlom, Science **327**, 1607 (2010).
4. A. F. Santander-Syro, O. Copie, T. Kondo, F. Fortuna, S. Pailhes, R. Weht, X. G. Qiu, F. Bertran, A. Nicolaou, A. Taleb-Ibrahimi, P. Le Fevre, G. Herranz, M. Bibes, N. Reyren, Y. Apertet, P. Lecoeur, A. Barthelemy, and M. J. Rozenberg, Nature **469**, 189 (2011).
5. W. Meevasana, P. D. C. King, R. H. He, S.-K. Mo, M. Hashimoto, A. Tamai, P. Songsiriritthigul, F. Baumberger, and Z.-X. Shen, Nat Mater **10**, 114 (2011).
6. M. Ben Shalom, M. Sachs, D. Rakhmilevitch, A. Palevski, and Y. Dagan, Phys. Rev. Lett. **104**, 126802 (2010).
7. A. D. Caviglia, M. Gabay, S. Gariglio, N. Reyren, C. Cancellieri, and J.-M. Triscone, Phys. Rev. Lett. **104**, 126803 (2010).
8. A. F. Santander-Syro, F. Fortuna, C. Bareille, T. C. Rödel, G. Landolt, N. C. Plumb, J. H. Dil, and M. Radović, Nat Mater **13**, 1085 (2014).
9. A. F. Santander-Syro, C. Bareille, F. Fortuna, O. Copie, M. Gabay, F. Bertran, A. Taleb-Ibrahimi, P. Le Fèvre, G. Herranz, N. Reyren, M. Bibes, A. Barthélémy, P. Lecoeur, J. Guevara, and M. J. Rozenberg, Phys. Rev. B **86**, 121107 (2012).
10. P. D. C. King, R. H. He, T. Eknapakul, P. Buaphet, S.-K. Mo, Y. Kaneko, S. Harashima, Y. Hikita, M. S. Bahramy, C. Bell, Z. Hussain, Y. Tokura, Z.-X. Shen, H. Y. Hwang, F. Baumberger, and W. Meevasana, Phys. Rev. Lett. **108**, 117602 (2012).
11. N. Reyren, M. Bibes, E. Lesne, J.-M. George, C. Deranlot, S. Collin, A. Barthélémy, and H. Jaffrès, Phys. Rev. Lett. **108**, 186802 (2012).
12. M. Kim, Y. Kozuka, C. Bell, Y. Hikita, and H. Y. Hwang, Phys. Rev. B **86**, 085121 (2012).
13. Y. A. Bychkov and E. I. Rashba, JETP Lett. **39**, 78 (1984).
14. G. Dresselhaus, Phys. Rev. **100**, 580 (1955).
15. R. Winkler, *Spin-Orbit Coupling Effects in Two-Dimensional Electron and Hole Systems* (Springer-Verlag, 2003).
16. Z. Zhong, A. Tóth, and K. Held, Phys. Rev. B **87**, 161102 (2013).
17. G. Khalsa, B. Lee, and A. H. MacDonald, Phys. Rev. B **88**, 041302 (2013).
18. P. Kim, K. T. Kang, G. Go, and J. H. Han, Phys. Rev. B **90**, 205423 (2014).
19. Y. Kim, R. M. Lutchyn, and C. Nayak, Phys. Rev. B **87**, 245121 (2013).
20. K. Shanavas and S. Satpathy, Phys. Rev. Lett. **112**, 086802 (2014).
21. S. R. Park, C. H. Kim, J. Yu, J. H. Han, and C. Kim, Phys. Rev. Lett. **107**, 156803 (2011).
22. B. Kim, C. H. Kim, P. Kim, W. Jung, Y. Kim, Y. Koh, M. Arita, K. Shimada, H. Namatame, M. Taniguchi, J. Yu, and C. Kim, Phys. Rev. B **85**, 195402 (2012).
23. J.-H. Park, C. H. Kim, J.-W. Rhim, and J. H. Han, Phys. Rev. B **85**, 195401 (2012).
24. E. A. Zhurova, Y. Ivanov, V. Zavodnik, and V. Tsirelson, Acta Crystallogr. Sect. B-Struct. **56**, 594 (2000).
25. T. Maekawa, K. Kurosaki, and S. Yamanaka, J. Alloy. Comp. **407**, 44 (2006).
26. G. Kresse and J. Hafner, Phys. Rev. B **47**, 558 (1993).
27. G. Kresse and J. Furthmüller, Phys. Rev. B **54**, 11169 (1996).
28. M. S. Scheurer and J. Schmalian, Nat Commun **6**, 6005 (2015).
29. J. Zhou, W.-Y. Shan, and D. Xiao, Phys. Rev. B **91**, 241302 (2015).
30. K. V. Shanavas, Z. S. Popović, and S. Satpathy, Phys. Rev. B **90**, 165108 (2014).
31. S. B. Chung, C. Chan, and H. Yao, Scientific Reports **6**, 25184 (2016).
32. H. Schulz, Europhys. Lett. **4**, 609 (1987).
33. I. Dzyaloshinskii, JETP Lett **46**, 118 (1987).
34. N. Furukawa, T. M. Rice, and M. Salmhofer, Phys. Rev. Lett. **81**, 3195 (1998).
35. J. González, Phys. Rev. B **78**, 205431 (2008).
36. R. Nandkishore, L. Levitov, and A. Chubukov, Nature Physics **8**, 158 (2012).
37. Z. Y. Meng, F. Yang, K.-S. Chen, H. Yao, and H.-Y. Kee, Phys. Rev. B **91**, 184509 (2015).

[38] H. Yao and F. Yang, Phys. Rev. B **92**, 035132 (2015).
[39] X. Chen, Y. Yao, H. Yao, F. Yang, and J. Ni, Phys. Rev. B **92**, 174503 (2015).
[40] K. Yoshimatsu, K. Horiba, H. Kumigashira, T. Yoshida, A. Fujimori, and M. Oshima, Science **333**, 319 (2011).
[41] S. Thiel, G. Hammerl, A. Schmehl, C. W. Schneider, and J. Mannhart, Science **313**, 1942 (2006).
[42] C. Rossel, B. Mereu, C. Marchiori, D. Caimi, M. Sousa, A. Guiller, H. Siegwart, R. Germann, J.-P. Locquet, J. Fompeyrine, D. J. Webb, C. Dieker, and J. W. Seo, Applied Physics Letters **89**, 053506 (2006).
[43] J. Ibañez Azpiroz, A. Eiguren, E. Y. Sherman, and A. Bergara, Phys. Rev. Lett. **109**, 156401 (2012).
[44] J.-H. Park, C. H. Kim, J.-W. Rhim, and J. H. Han, Phys. Rev. B **85**, 195401 (2012).
[45] P. E. Blöchl, Phys. Rev. B **50**, 17953 (1994).
[46] J. P. Perdew, A. Ruzsinszky, G. I. Csonka, O. A. Vydrov, G. E. Scuseria, L. A. Constantin, X. Zhou, and K. Burke, Phys. Rev. Lett. **100**, 136406 (2008).
[47] N. Marzari and D. Vanderbilt, Phys. Rev. B **56**, 12847 (1997).
[48] I. Souza, N. Marzari, and D. Vanderbilt, Phys. Rev. B **65**, 035109 (2001).
[49] A. A. Mostofi, J. R. Yates, Y.-S. Lee, I. Souza, D. Vanderbilt, and N. Marzari, Computer Physics Communications **178**, 685 (2008).
[50] A. Stroppa, D. Di Sante, P. Barone, M. Bokdam, G. Kresse, C. Franchini, M.-H. Whangbo, and S. Picozzi, Nat Commun **5**, 5900 (2014).
[51] P. Yu and M. Cardona, *Fundamentals of Semiconductors: Physics and Materials Properties* (Springer-Verlag, 2010).